Sonoelasticity imaging: Theory and experimental verification

L. Gao, K. J. Parker, and S. K. Alam
Department of Electrical Engineering, Center for Biomedical Ultrasound and Department of Radiology, University of Rochester, Rochester, New York 14627

R. M. Lerner
Department of Diagnostic Radiology, Rochester General Hospital, Rochester, New York 14621

(Received 7 April 1994; accepted for publication 3 February 1995)

Sonoelasticity is a rapidly evolving medical imaging technique for visualizing hard tumors in tissues. In this novel diagnostic technique, a low-frequency vibration is externally applied to excite internal vibrations within the tissue under inspection. A small stiff inhomogeneity in a surrounding tissue appears as a disturbance in the normal vibration eigenmode pattern. By employing a properly designed Doppler detection algorithm, a real-time vibration image can be made. A theory for vibrations, or shear wave propagation in inhomogeneous tissue has been developed. A tumor is modeled as an elastic inhomogeneity inside a lossy homogeneous elastic medium. A vibration source is applied at a boundary. The solutions for the shear wave equation have been found both for the cases with tumor (inhomogeneous case) and without tumor (homogenous case). The solutions take into account varying parameters such as tumor size, tumor stiffness, shape of vibration source, lossy factor of the material, and vibration frequency. The problem of the lowest detectable change in stiffness is addressed using the theory, answering one of the most critical questions in this diagnostic technique. Some experiments were conducted to check the validity of the theory, and the results showed a good correspondence to the theoretical predictions. These studies provide basic understanding of the phenomena observed in the growing field of clinical Sonoelasticity imaging for tumor detection.

PACS numbers: 43.80.Qf, 43.80.Jz, 43.80.Vj

LIST OF SYMBOLS

ξ	displacement field vector
ξ_l	longitudinal component of the displacement field vector
ξ_s	shear component of the displacement field vector
ρ	density
E	Young's modulus (stiffness)
ν	Poisson's ratio
C_l	speed of the longitudinal wave
C_s	speed of the shear wave
w_0	angular vibration frequency
Q_0	Q factor of the system

INTRODUCTION

Palpation is a traditional tumor detection method that identifies abnormal regions of increased stiffness (elasticity). But the method is limited to only those tumors which occur close to an accessible surface. Conventional medical imaging, including MRI, CT, mammography, and gray scale ultrasound, is insensitive to stiffness as an imaging parameter and often fails to reveal the extent or existence of tumors which, upon pathologic examination, are found to be palpably more stiff than surrounding normal tissues.

Sonoelasticity imaging is a method of "remote palpation" that identifies hard tumors. This technique combines externally applied vibrations with Doppler detection of the response throughout tissue, to indicate abnormal regions. We define Sonoelasticity as consisting of sinusoidal steady state vibrations, with externally applied stimulus, and production of modal patterns in some organs, and Doppler detection of vibration to generate an image. Sonoelasticity imaging is related to three much larger, older, and somewhat overlapping fields:

(1) the study of vibrating targets using coherent radiation (laser, sonar, and ultrasound) (Holen *et al.*, 1985; Cox and Rogers, 1987; Taylor, 1976, 1981),

(2) the study of tissue elastic constants (biomechanics) (Fung, 1981; Levinson, 1987; Parker *et al.*, 1993), and

(3) the study of tissue motion using imaging systems (ultrasound, MRI, stroboscopes, and others) (Oestreicher, 1951; Von Gierke *et al.*, 1952; Wilson and Robinson, 1982; Dickinson and Hill, 1982; Eisenscher *et al.*, 1983; Bimholz and Farrell, 1985; Tristam *et al.*, 1986, 1988; Axel and Dougherty, 1989; Adler *et al.*, 1989, 1990).

To accurately interpret sonoelasticity images, we must understand the nature of tissue vibrations under different circumstances. There has been some preliminary work on vibration modal patterns in tissue (Lerner and Parker, 1987a, 1987b; Lerner *et al.*, 1988, 1990; Parker *et al.*, 1990; Parker and Lerner, 1992; Lee *et al.*, 1991; Huang, 1990; Gao *et al.*, 1993). Other vibration techniques (Krouskop *et al.*, 1987; Yamakoshi *et al.*, 1990), and also an important class of static and quasistatic techniques have been independently developed by Ophir and others (Ophir *et al.*, 1991; Ponnekanti *et al.*, 1992; Yemelyanov *et al.*, 1992; Céspedes *et al.*, 1993;

 0001-4966/95/97(6)/3875/12/$6.00

O'Donnell *et al.*, 1993; Skovoroda *et al.*, 1994; O'Donnell *et al.*, 1994). In addition, other approaches to tissue motion and elasticity measurements have been proposed (Meunier *et al.*, 1989; Ryan *et al.*, 1992, 1993; Javier and Pedersen, 1994).

A novel theory for vibrations or shear wave propagation in inhomogeneous tissue is developed in this paper. The theory describes the characteristic patterns we expect to see in a sonoelasticity image, especially for tumor recognition. Phantom and *in vivo* experiments were conducted to corroborate the theory.

I. THEORY

A. Tumor model

We begin by modeling a tumor as an elastic inhomogeneity inside a lossy homogeneous elastic medium. For example, the media stiffness is a constant E_0, except the small area around (x_0,y_0) has the stiffness E_0+E'. When we apply boundary conditions and a driving vibration force, we want to compare the vibration patterns of this medium with and without the inhomogeneity.

B. Displacement wave equation

We start from the basic field wave equations. For a general linear and isotropic material, the displacement field vector $\boldsymbol{\xi}(\mathbf{x},t)$ satisfies the following equation (Landau and Liftshitz, 1970):

$$\frac{E}{2(1+\nu)}\nabla^2\boldsymbol{\xi}+\frac{E}{2(1+\nu)(1-2\nu)}\nabla\nabla\cdot\boldsymbol{\xi}=\rho\frac{\partial^2\boldsymbol{\xi}}{\partial t^2}. \quad (1)$$

The displacement field vector $\boldsymbol{\xi}$ can be decomposed into longitudinal and shear components (Φ and $\mathbf{A}$ are the potential functions for longitudinal and shear components, respectively)

$$\boldsymbol{\xi}=\nabla\Phi+\nabla\times\mathbf{A} \quad (2)$$

$$=\boldsymbol{\xi}_l+\boldsymbol{\xi}_s. \quad (3)$$

The two components satisfy, respectively,

$$\nabla\times\boldsymbol{\xi}_l=0, \quad (4a)$$

$$\nabla\cdot\boldsymbol{\xi}_s=0. \quad (4b)$$

As derived in the reference (Landau and Liftshitz, 1970), Eq. (1) will give the homogeneous longitudinal and shear wave equations

$$\nabla^2\boldsymbol{\xi}_l-\frac{1}{C_l^2}\frac{\partial^2\boldsymbol{\xi}_l}{\partial t^2}=0, \quad (5a)$$

$$\nabla^2\boldsymbol{\xi}_s-\frac{1}{C_s^2}\frac{\partial^2\boldsymbol{\xi}_s}{\partial t^2}=0, \quad (5b)$$

where

$$C_l^2=\frac{E}{2\rho(1+\nu)(1-2\nu)}, \quad (6a)$$

$$C_s^2=\frac{E}{2\rho(1+\nu)}. \quad (6b)$$

Inside both the homogeneous region (tissue) and the inhomogeneous region (tumor), the field vector satisfies the same wave equations (5), but with different C_l and C_s. We assume that ν and ρ do not vary significantly for tumor and normal tissues. The most distinguishable mechanical property that separates tumor from normal tissue is the stiffness E (Parker *et al.*, 1990, 1993). Over the whole medium, we can write E as

$$E(\mathbf{x})=E_0+E'(\mathbf{x}), \quad (7)$$

with

$$E'(\mathbf{x})=\begin{cases}E', & \text{for tumor area } L_a'L_b' \text{ centered at } (x_0,y_0),\\ 0, & \text{for surrounding tissue.}\end{cases} \quad (8)$$

Then we can derive a general expression for the speed of the shear wave:

$$\begin{aligned}C_s^2(\mathbf{x})&=E(\mathbf{x})/(2\rho(1+\nu))\\ &=E_0/(2\rho(1+\nu))+E'(\mathbf{x})/(2\rho(1+\nu))\\ &=(1+E'(\mathbf{x})/E_0)E_0/(2\rho(1+\nu)).\end{aligned} \quad (9)$$

If we denote

$$C_0^2=E_0/(2\rho(1+\nu)), \quad (10)$$

$$\gamma(\mathbf{x})=E'(\mathbf{x})/E_0, \quad (11)$$

then expression (9) could be simplified as

$$C_s^2(\mathbf{x})=C_0^2(1+\gamma(\mathbf{x})) \quad (12)$$

and $\gamma(\mathbf{x})$ should satisfy

$$\gamma(\mathbf{x})=\begin{cases}E'/E=\gamma, & \text{in tumor area } L_a'L_b' \text{ around } (x_0,y_0),\\ 0, & \text{everywhere else.}\end{cases} \quad (13)$$

So instead of writing two shear wave equations for both the homogeneous and inhomogeneous region, we may write one equation for the entire medium:

$$\nabla^2\boldsymbol{\xi}_s-\frac{1}{C_0^2(1+\gamma(\mathbf{x}))}\frac{\partial^2\boldsymbol{\xi}_s}{\partial t^2}=0. \quad (14)$$

We have chosen to concentrate on shear waves, since low-frequency longitudinal waves have wavelengths that are too large compared to organs of interest at the frequencies used in sonoelasticity imaging (Parker and Lerner, 1992). Furthermore, for simplicity, we will consider the two-dimensional case. If we denote this two-dimensional plane as the X-Y plane, we will only consider the Z component of the displacement vector $\boldsymbol{\xi}_s$. Thus the letter ξ represents the z component of displacement in all later discussions. The solutions for rectangular enclosures are given for simplicity, although these can be expanded to spherical, cylindrical, elliptical, and other regular geometries. Four cases are given to cover a range of complexity, and build an understanding of the simpler cases.

C. Case one

The case of the homogeneous, lossless medium without source: For a homogeneous rectangle, on all four boundaries $x=0$, $x=L_a$, $y=0$, and $y=L_b$, the displacement is prescribed as $\xi=0$ on rigid walls.

Solution: Begin with Eq. (14). In this case the material is homogeneous, $\gamma(\mathbf{x})=0$ over the rectangle, so the wave equation becomes

$$\nabla^2\xi-\frac{1}{C_0^2}\frac{\partial^2\xi}{\partial t^2}=0. \tag{15}$$

The sinusoidal steady-state solution is well known as

$$\xi=\xi_0\exp(iw_0t)\sin(k_mx)\sin(k_ny), \tag{16}$$

with $k_m=m\pi/L_a$, $k_n=n\pi/L_b$ (m and n are integers), and $w_0^2=C_0^2(k_m^2+k_n^2)$. Thus eigenmodes occur at predictable eigenfrequencies.

D. Case two

The case of the homogeneous, lossy medium with a vibration source on one side: For a homogeneous rectangle, on boundaries $x=0$, $y=0$, and $y=L_b$, the displacement ξ is zero. On the fourth boundary $x=L_a$, $\xi=\epsilon_0\times\exp(iw_0t)\sin(k_Jy)$. Here $k_J=J\pi/L_b$, J is an integer, and ϵ_0 is a real constant. The material is lossy.

Solution: The term $\gamma(\mathbf{x})=0$ throughout the homogeneous medium. As the system is lossy, a relaxation term can be included in Eq. (14) (Kinsler *et al.*, 1982):

$$\nabla^2\xi-\frac{1}{C_0^2}\frac{\partial^2\xi}{\partial t^2}-\frac{R}{\rho C_0^2}\frac{\partial\xi}{\partial t}=0 \tag{17}$$

(with $w_0\rho/R=Q_0$, which is the Q factor of the system at w_0).

Assuming sinusoidal dependence $\xi=\xi\exp(iw_0t)$, the above equation becomes

$$\nabla^2\xi+K^2\xi-(iK^2/Q_0)\xi=0, \tag{18}$$

with $K=w_0/C_0$, which is the vibration wave number.

Given the boundary condition, we know the form of the solution should be

$$\xi=E_0\sin[(k_m+i\alpha)x]\sin(k_Jy). \tag{19}$$

Substituting this into the wave equation (18) and the source term, we find

$$k_m=(1/\sqrt{2})\sqrt{k_r+\sqrt{k_r^2+K^4/Q_0^2}}, \tag{20a}$$

$$\alpha=-K^2/2k_mQ_0, \tag{20b}$$

$$E_0=\frac{\epsilon_0}{\sin[(k_m+i\alpha)L_a]}, \tag{20c}$$

with $k_r=K^2-k_J^2$.

We could rewrite the solution given by Eq. (19) in the conventional exponential form:

$$\xi=\frac{\epsilon_0}{2}\exp(iw_0t)\sin(k_Jy)\times\frac{\exp(ik_mx-\alpha x)-\exp(-ik_mx+\alpha x)}{\exp(ik_mL_a-\alpha L_a)-\exp(-ik_mL_a+\alpha L_a)}. \tag{21}$$

Separating the real and imaginary part, Eq. (21) becomes

$$\xi=\epsilon_0\sin(k_Jy)[(G+iH)/2F]\exp(iw_0t), \tag{22}$$

with

$$F=((\exp(-\alpha L_a)-\exp(\alpha L_a))\cos(k_mL_a))^2+((\exp(-\alpha L_a)+\exp(\alpha L_a))\sin(k_mL_a))^2, \tag{23a}$$

$$G=(\exp(-\alpha L_a)-\exp(\alpha L_a))(\exp(-\alpha x)-\exp(\alpha x))\cos(k_mL_a)\cos(k_mx)+(\exp(-\alpha L_a)+\exp(\alpha L_a))(\exp(-\alpha x)+\exp(\alpha x))\sin(k_mL_a)\sin(k_mx), \tag{23b}$$

$$H=(\exp(-\alpha L_a)-\exp(\alpha L_a))(\exp(-\alpha x)+\exp(\alpha x))\cos(k_mL_a)\sin(k_mx)-(\exp(-\alpha L_a)+\exp(\alpha L_a))(\exp(-\alpha x)-\exp(\alpha x))\sin(k_mL_a)\cos(k_mx). \tag{23c}$$

Only the real part of ξ is the solution, which is

$$\mathrm{Re}(\xi)=\epsilon_0\sin(k_Jy)\,\frac{G\cos(w_0t)-H\sin(w_0t)}{2F}. \tag{24}$$

Since ultrasound Doppler devices can easily detect the vibration amplitude, we are also interested in that function of position:

$$|\mathrm{Re}(\xi)|=\epsilon_0\sin(k_Jy)(\sqrt{G^2+H^2}/2F). \tag{25}$$

E. Case three

The case of the inhomogeneous, lossy medium with a vibration source: Again we begin with a rectangle with dimension $L_a\times L_b$. On the boundaries $x=0$, $y=0$, and $y=L_b$, the boundary condition is $\xi=0$. The fourth boundary $x=L_a$ satisfies $\xi=\epsilon_0\exp(iw_0t)\sin(k_Jy)$. ϵ_0 is a real constant. The material is lossy. The stiffness of the inhomogeneous area is E_0+E' with dimension $L_a'\times L_b'$ (assumed small), which is located at (x_0,y_0).

Solution: Combining the lossy term of Eq. (17) with the inhomogeneous wave equation (14) produces

$$\nabla^2\xi-\frac{1}{C_0^2(1+\gamma(\mathbf{x}))}\frac{\partial^2\xi}{\partial t^2}-\frac{R}{\rho C_0^2(1+\gamma(\mathbf{x}))}\frac{\partial\xi}{\partial t}=0 \tag{26}$$

(with $w_0\rho/R=Q_0$, which is the Q factor of the system at w_0).

Assuming the sinusoidal time dependence $\xi=\xi\exp(iw_0t)$, the equation above becomes

$$\nabla^2\xi+\frac{K^2}{[1+\gamma(\mathbf{x})]}\xi-\frac{iK^2}{Q_0[1+\gamma(\mathbf{x})]}\xi=0, \tag{27}$$

where $K=w_0/C_0$ and $Q_0=w_0\rho/R$.

Without changing the equation above, we rewrite it as

$$\nabla^2\xi+K^2\xi-\frac{iK^2}{Q_0}\xi=\frac{K^2\gamma(\mathbf{x})}{1+\gamma(\mathbf{x})}\xi-\frac{iK^2}{Q_0}\frac{\gamma(\mathbf{x})}{1+\gamma(\mathbf{x})}\xi. \quad (28)$$

Denoting $\beta(\mathbf{x})=[\gamma(\mathbf{x})]/[1+\gamma(\mathbf{x})]$, and recalling the definition of $\gamma(\mathbf{x})$ given by Eq. (13), we summarize the behavior of $\beta(\mathbf{x})$:

$$\beta(\mathbf{x})=\begin{cases}\gamma/(1+\gamma), & \text{in the area } L_a'L_b' \text{ around } (x_0,y_0),\\ 0, & \text{everywhere else.}\end{cases} \quad (29)$$

Splitting ξ into incident and scattered waves,

$$\xi=\xi_i+\xi_s, \quad (30)$$

where ξ_i stands for the incident wave and ξ_s for the scattered wave. ξ_i satisfies the homogeneous lossy wave equation (18), which we rewrite for the sake of emphasis

$$\nabla^2\xi_i+K^2\xi_i-(iK^2/Q_0)\xi_i=0. \quad (31)$$

Substituting Eqs. (30) and (31) into Eq. (26), the latter becomes

$$\nabla^2\xi_s+K^2\xi_s-\frac{iK^2}{Q_0}\xi_s=\beta(\mathbf{x})K^2\left(1-\frac{i}{Q_0}\right)(\xi_i+\xi_s). \quad (32)$$

As $\beta(\mathbf{x})$ is zero everywhere, except around (x_0,y_0) where it is $\gamma/(1+\gamma)$, we may assume that the scattered wave is much smaller than the incident wave: $\xi_s \ll \xi_i$, and discard the term $\beta(\mathbf{x})K^2(1-i/Q_0)\xi_s$. [This is analogous to the Born approximation for longitudinal wave scattering (Morse and Ingard, 1968).] This results in

$$\nabla^2\xi_s+K^2\xi_s-\frac{iK^2}{Q_0}\xi_s=\beta(\mathbf{x})K^2\left(1-\frac{i}{Q_0}\right)\xi_i. \quad (33)$$

Equation (33) is the governing equation for shear wave propagation in a lossy, inhomogeneous, elastic medium under the "sonoelastic Born approximation." Case two gives the solution of the incident wave, with the same boundary conditions defined as above. So our problem now is to obtain the solution of the scattered wave ξ_s.

As $\xi=\xi_i+\xi_s$, ξ_s should have the following boundary condition: on all four boundaries, $\xi_s=0$. With this boundary condition, we know that the solution of ξ_s can be completely determined by the following series expansion:

$$\xi_s=\sum_{pq}(A_{pq}+iB_{pq})\sin(k_px)\sin(k_qy), \quad (34)$$

where $k_p=p\pi/L_a$, $k_q=q\pi/L_b$, and p and q are integers.

Substituting the ξ_s given by Eq. (34) into the left-hand side of Eq. (33), we have

$$\text{LHS}=\left(\nabla^2+K^2-\frac{iK^2}{Q_0}\right)\sum_{pq}(A_{pq}+iB_{pq})\times\sin(k_px)\sin(k_qy). \quad (35)$$

Expand the right-hand side of Eq. (33) into a series also:

$$\text{RHS}=K^2\beta(\mathbf{x})\left(1-\frac{i}{Q_0}\right)\xi_i=\sum_{pq}C_{pq}\sin(k_px)\sin(k_qy), \quad (36)$$

with

$$C_{pq}=\frac{4}{L_aL_b}\int_0^{L_a}\int_0^{L_b}K^2\beta(\mathbf{x})\left(1-\frac{i}{Q_0}\right)\times\xi_i\sin(k_px)\sin(k_qy)dx\,dy. \quad (37)$$

As $\beta(\mathbf{x})$ is zero except in the small area $L_a'L_b'$ around (x_0,y_0), we assume that ξ_i and the two sinusoidal functions are essentially constant over this small region of integration. As a preliminary approximation, we use their values at the point (x_0,y_0) to carry out the integration. So the integral becomes

$$C_{pq}=\frac{4L_a'L_b'}{L_aL_b}K^2\frac{\gamma}{1+\gamma}\left(1-\frac{i}{Q_0}\right)\xi_i(x_0,y_0)\times\sin(k_px_0)\sin(k_qy_0), \quad (38)$$

where $\xi_i(x_0,y_0)$ represents the value of ξ_i at the point (x_0,y_0).

We have the expression of ξ_i given by Eq. (22) in case two, so C_{pq} is known. Setting LHS=RHS, expressions for A_{pq} and B_{pq} are produced:

$$A_{pq}=\epsilon_0\frac{2L_a'L_b'}{L_aL_b}\frac{\gamma}{1+\gamma}\sin(k_Jy_0)\times\frac{K^2[(K^2-k_p^2-k_q^2)G'(x_0,y_0)-(K^2/Q_0)H'(x_0,y_0)]}{F[(K^2-k_p^2-k_q^2)^2+(K^2/Q_0)^2]}\times\sin(k_px_0)\sin(k_qy_0), \quad (39a)$$

$$B_{pq}=\epsilon_0\frac{2L_a'L_b'}{L_aL_b}\frac{\gamma}{1+\gamma}\sin(k_Jy_0)\times\frac{K^2[(K^2-k_p^2-k_q^2)H'(x_0,y_0)+(K^2/Q_0)G'(x_0,y_0)]}{F[(K^2-k_p^2-k_q^2)^2+(K^2/Q_0)^2]}\times\sin(k_px_0)\sin(k_qy_0), \quad (39b)$$

with

$$G'(x_0,y_0)=G(x_0,y_0)+\frac{H(x_0,y_0)}{Q_0}, \quad (40a)$$

$$H'(x_0,y_0)=H(x_0,y_0)-\frac{G(x_0,y_0)}{Q_0}. \quad (40b)$$

$G(x_0,y_0)$ and $H(x_0,y_0)$ represent the value of G and H at the point (x_0,y_0). The expression of G, H, and F are given in case two by Eq. (23).

So we have the solution for ξ_s, and also that for ξ_i given by Eq. (22):

$$\xi_s=\sum_{pq}(A_{pq}+iB_{pq})\sin(k_px)\sin(k_qy), \quad (41)$$

$$\xi_i=\epsilon_0\sin(k_Jy)\,[(G+iH)/2F]. \quad (42)$$

The total wave will be

$$\xi=(\xi_i+\xi_s)\exp(iw_0t). \quad (43)$$

Only the real part of the solution is of interest, which is

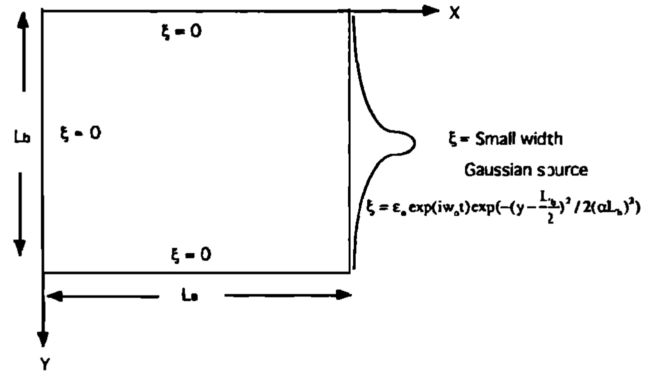

FIG. 1. Boundary conditions of case four, where a Gaussian vibration source is applied to a two-dimensional object.

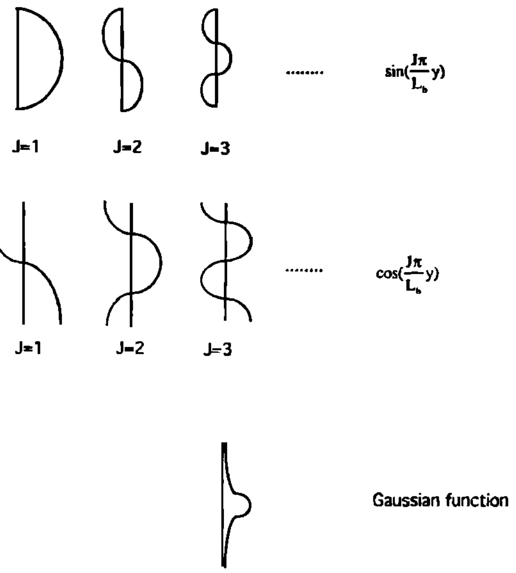

FIG. 2. Comparison of the functions that are used to compose the Gaussian source.

$$\begin{aligned}\mathrm{Re}(\xi)=&\left(\epsilon_0\sin(k_Jy)\,\frac{G}{2F}\right.\\&\left.+\sum_{pq}A_{pq}\sin(k_px)\sin(k_qy)\right)\cos(w_0t)\\&-\left(\epsilon_0\sin(k_Jy)\,\frac{H}{2F}\right.\\&\left.+\sum_{pq}B_{pq}\sin(k_px)\sin(k_qy)\right)\sin(w_0t).\end{aligned}\tag{44}$$

Also of interest is the amplitude of the vibration,

$$\begin{aligned}\mathrm{Amp}_{\mathrm{Re}(\xi)}=&\left[\left(\epsilon_0\sin(k_Jy)\,\frac{G}{2F}\right.\right.\\&\left.+\sum_{pq}A_{pq}\sin(k_px)\sin(k_qy)\right)^2\\&+\left(\epsilon_0\sin(k_Jy)\,\frac{H}{2F}\right.\\&\left.\left.+\sum_{pq}B_{pq}\sin(k_px)\sin(k_qy)\right)^2\right]^{1/2}.\end{aligned}\tag{45}$$

F. Case four

The case of the inhomogeneous, lossy medium with Gaussian source (shown in Fig. 1): Based on case three, we model the vibration source as Gaussian extended source, which is more plausible for some experimental setups.

We have a rectangle with dimension $L_a\times L_b$. On the boundaries $x=0$, $y=0$, and $y=L_b$, the boundary condition is $\xi=0$. The fourth boundary $x=L_a$ satisfies $\xi=\epsilon_0\exp(iw_0t)\exp[-(y-L_b/2)^2/2(\alpha L_b)^2]$. α is a small number (no more than 0.11), so the source is a small width Gaussian. ϵ_0 is a real constant. The material is lossy. The inhomogeneous area is around (x_0,y_0).

Solution: The approach is to decompose the Gaussian boundary condition into a sinusoidal boundary condition, obtain the solution for each sinusoidal component, and then apply superposition. In this case, we may decompose the Gaussian function into

$$\begin{aligned}&\exp\left[-\left(y-\frac{L_b}{2}\right)^2\Big/2(\alpha L_b)^2\right]\\&\quad=\sum_{J=0}^{\infty}\left[C_J\sin\left(\frac{J\pi}{L_b}\,y\right)+D_J\cos\left(\frac{J\pi}{L_b}\,y\right)\right].\end{aligned}\tag{46}$$

If the Gaussian is centered on the midpoint $y=L_b/2$, and is assumed to approach zero at the extremes of the rectangle, then we could decompose that Gaussian only into sine functions (refer to Fig. 2):

$$\exp\left[-\left(y-\frac{L_b}{2}\right)^2\Big/2(\alpha L_b)^2\right]\cong\sum_{J=0}^{\infty}C_J\sin\left(\frac{J\pi}{L_b}\,y\right).\tag{47}$$

C_J is given by

$$\begin{aligned}C_J\cong&\frac{2}{L_b}\int_0^{L_b}\sin\left(\frac{J\pi}{L_b}\,y\right)\\&\times\exp\left[-\left(y-\frac{L_b}{2}\right)^2\Big/2(\alpha L_b)^2\right]dy.\end{aligned}\tag{48}$$

Changing the integral variable $y-L_b/2\rightarrow y$, the above equation becomes

$$C_J\cong\frac{2}{L_b}\int_{-L_b/2}^{L_b/2}\sin\left[\frac{J\pi}{L_b}\left(y+\frac{L_b}{2}\right)\right]\exp\left(\frac{-y^2}{2(\alpha L_b)^2}\right)dy.\tag{49}$$

As α is assumed to be no more than 0.11, the exponential in the integral goes almost to zero at $y=\pm L_b/2$, and it becomes even smaller when $|y|>L_b/2$. So as a reasonable approximation, we could extend the limit to $\pm\infty$ with little effect on the value of C_J:

$$C_J \cong \frac{2}{L_b} \int_{-\infty}^{\infty} \sin\left[\frac{J\pi}{L_b}\left(y+\frac{L_b}{2}\right)\right] \exp\left(\frac{-y^2}{2(\alpha L_b)^2}\right) dy. \tag{50}$$

Now this is in the form of a known integration (Gradshteyn and Ryzhik, 1965):

$$\int_{-\infty}^{\infty} \sin(p(x+\phi))\exp(-q^2x^2)dx$$

$$= \frac{\sqrt{\pi}}{q} \sin(p\phi)\exp\left(-\frac{p^2}{4q^2}\right). \tag{51}$$

So the expression of C_J is

$$C_J = 2\alpha\sqrt{2\pi} \sin\left(\frac{J\pi}{2}\right)\exp\left(-\frac{J^2\pi^2\alpha^2}{2}\right). \tag{52}$$

Note that C_J is 0 for $J=0,2,4,\ldots$. That is easily understood by analyzing the symmetry property. Our Gaussian function is even symmetric with respect to the point $y=L_b/2$, so we expect the odd-symmetric components to be zero. Please note that

$$C_J \to 0 \quad \text{as } J \to \infty$$

and the decay is square exponential, which provides rapid convergence. So in computer simulation, we could truncate the series (47) at a reasonable J'.

For the sake of emphasis, we rewrite the decomposition equation (47) here:

$$\epsilon_0 \exp[iw_0t]\exp\left[-\left(y-\frac{L_b}{2}\right)^2 \Big/ 2(\alpha L_b)^2\right]$$

$$\cong \epsilon_0 \exp(iw_0t)\sum_{J=1}^{\infty} C_{2J-1} \sin\left(\frac{(2J-1)\pi}{L_b} y\right). \tag{53}$$

Case three gives the solution when the source term is a sine function $\epsilon_0 \exp(iw_0t)\sin[(J\pi/L_b)y]$. So the solution for the Gaussian source is easily obtained by adding up the results of those sine functions, weighted by the coefficient C_J. Using Eq. (43), our final solution is

$$\xi = \exp(iw_0t)\sum_{J=1}^{\infty} C_{2J-1}(\xi_{(2J-1)i}+\xi_{(2J-1)s}). \tag{54}$$

Here $\xi_{(2J-1)i}$ means the incident wave of the $(2J-1)$th component, and $\xi_{(2J-1)s}$ the scattered wave of the $(2J-1)$th component. The expressions below also contain the index $(2J-1)$, and it is understood as indicating the $(2J-1)$th component.

Only the real part is the solution, which is

$$\begin{aligned}\mathrm{Re}(\xi) = {} & \cos(w_0t)\sum_{J=1}^{\infty} C_{2J-1}\left(\epsilon_0 \sin(k_{2J-1}y)\,\frac{G_{2J-1}}{2F_{2J-1}} + \sum_{pq} A_{(2J-1)pq} \sin(k_{(2J-1)p}x)\sin(k_{(2J-1)q}y)\right) \\ & - \sin(w_0t)\sum_{J=1}^{\infty} C_{2J-1}\left(\epsilon_0 \sin(k_{2J-1}y)\,\frac{H_{2J-1}}{2F_{2J-1}} + \sum_{pq} B_{(2J-1)pq} \sin(k_{(2J-1)p}x)\sin(k_{(2J-1)q}y)\right).\end{aligned} \tag{55}$$

The amplitude is given by

$$\begin{aligned}|\mathrm{Re}(\xi)| = \Bigg\{ & \left[\sum_{J=1}^{\infty} C_{2J-1}\left(\epsilon_0 \sin(k_{2J-1}y)\,\frac{G_{2J-1}}{2F_{2J-1}} + \sum_{pq} A_{(2J-1)pq} \sin(k_{(2J-1)p}x)\sin(k_{(2J-1)q}y)\right)\right]^2 \\ & + \left[\sum_{J=1}^{\infty} C_{2J-1}\left(\epsilon_0 \sin(k_{2J-1}y)\,\frac{H_{2J-1}}{2F_{2J-1}} + \sum_{pq} B_{(2J-1)pq} \sin(k_{(2J-1)p}x)\sin(k_{(2J-1)q}y)\right)\right]^2\Bigg\}^{1/2}.\end{aligned} \tag{56}$$

G. Examples

To visualize the vibration solutions derived above, we simulated some solutions to the different cases (refer to Fig. 3). The first three are for the case of a homogeneous, lossy medium with a Gaussian source. The last three are the case of an inhomogeneous, lossy medium with a Gaussian source, using the same parameters as the first three, except for the inclusion of a discrete inhomogeneity. The parameters are selected to coincide with phantom experiments given in Sec. II of this paper.

A rectangle with dimensions $L_a \times L_b = 5$ cm$\times$4.5 cm is considered. On the boundaries $x=0$, $y=0$, and $y=L_b$, the boundary condition is $\xi=0$. The fourth boundary $x=L_a$ satisfies $\xi=\epsilon_0 \exp(iw_0t)\exp[-(y-L_b/2)^2/2(\alpha L_b)^2]$, where $\alpha=0.06$. The medium is lossy, where Q_0 of the system is 4.0. The speed of sound, C_0, is set to 3.79 m/s (Huang, 1990). For the inhomogeneous case, the inhomogeneity is located at $x=1.9$ cm, $y=3.3$ cm, and it has a area of $L_a'L_b'$, which is 0.013 of L_aL_b. The tumor stiffness E_0' is $8\times E_0$, the stiffness of the surrounding tissue. The source frequencies are 60, 100, and 200 Hz, respectively.

For the homogeneous cases, the simple eigenmodes are clearly seen to be a function of frequency, and the damping results in a loss of amplitude away from the source (on the right-hand side). We could see very clearly that for the inhomogeneous cases, the "tumor" region has a localized distur-

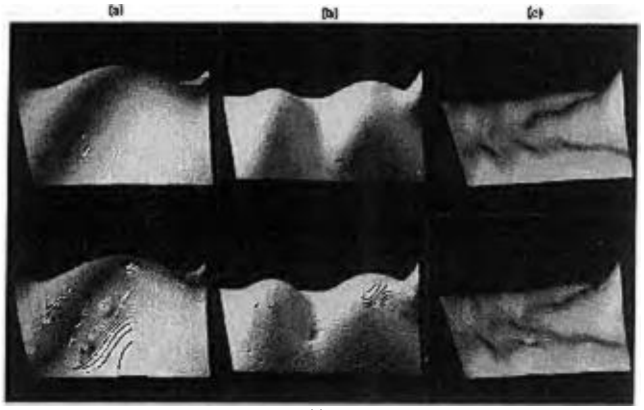

FIG. 3. Shear wave vibration (amplitude) in a lossy elastic medium with Gaussian source. Vibration is applied at the right-hand boundary. (a)–(c) are the modal patterns in a homogeneous medium, with the vibration frequencies of 60, 100, and 200 Hz, respectively. (d)–(f) are vibrations in a similar medium with a hard tumor (discrete inhomogeneity) located in the lower middle region. This inhomogeneous medium is vibrated at the same three frequencies as in the homogeneous examples. Note the distinct circular defect produced by the tumor.

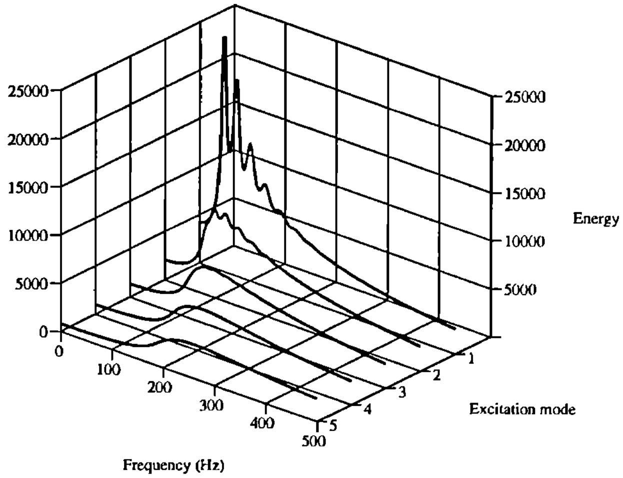

FIG. 4. Energy curve showing the frequency response of a lossy, homogeneous elastic medium with different source excitation modes.

bance in the vibration pattern, as compared with the corresponding homogeneous case.

H. Energy curve

To gain a better understanding of the system response under different source frequencies and boundary conditions, we also plotted the so-called energy or frequency response curve.

The energy of the vibrating system is proportional to the sum of the square of the amplitude at every point. Using Eq. (25), we plotted the sum of amplitude squared versus the source frequency f_0 ($f_0=w_0/2\pi$), and the excitation mode J that controls k_J [and the boundary condition $\xi=\epsilon_0 \exp(iw_0t)\sin(k_Jy)$]. The model is taken from case two, where a homogeneous rectangle $L_a\times L_b=5$ cm$\times$6 cm, on boundaries $x=0$, $y=0$, and $y=L_b$, the displacement ξ is zero. On the fourth boundary $x=L_a$, $\xi=\epsilon_0 \times\exp(iw_0t)\sin(k_Jy)$. The material lossy factor is 4.0.

The results are given in Fig. 4 for constant displacement ϵ_0 of the source. This demonstrates that the largest response is obtained from the lowest order modes, where the frequency and source shape match the natural eigenmode of that eigenfrequency. At the higher frequencies, the loss mechanisms damp the total energy and the response.

II. EXPERIMENTS AND COMPUTER SIMULATIONS

A. Phantom experiments

Phantoms were used to study the possibility of tumor detection by sonoelasticity. As the theory given earlier is two dimensional, we constructed long rectangular phantoms. The dimension of the phantom was about 5 cm$\times$5 cm$\times$30 cm (width$\times$height$\times$length). Two kinds of experiments were conducted. The first employed a homogeneous phantom; the second included an inhomogeneity. The homogeneous phantom was constructed using 500 g of water, 500 g of ethylene glycol, 70 g of gelatin, 100 g of glycerol, 100 g of formalin, and 10 g of barium sulfate. A gel phantom (1.5% agar, 1.5% gelatin, 0.1% barium sulfate) was used for the second experiment. A harder gel tube (3% agar, 3% gelatin, 0.1% barium sulfate) was buried in the phantom as the inhomogeneity. The Young's modulus of the hard gel tube was about 4$\times$ that of the phantom (Huang, 1990). The diameter of the hard gel tube was 0.6 cm. Figure 5 shows a sketch of the inhomogeneous phantom.

A sketch of the experiment setup is drawn in Fig. 6. The ultrasound transducer, a linear array 7.5 MHz (L738) from Acuson (Mountain View, CA), was positioned at 45° with respect to the top ($Y=0$ cm plane) boundary, and so was able to detect the vibrations of the X-Y plane along the Z axis. The vibration was applied by a minishaker type 4810 (Brüel & Kjær, Denmark) from the side of the phantom (the $X=5$ cm face in Fig. 6). The vibration direction was along the Z axis. The diameter of the tip of the vibrator was about 0.5 cm, and the contact area extended 2 cm in the Z axis. Rigid surfaces covered the phantom to ensure a rigid boundary condition, except for the location of the imaging transducer (center of $Y=0$ cm plane) and the vibration source (center of $X=5$ cm plane). The amplifier was a power amplifier type 2706 (Brüel & Kjær, Denmark).

The real-time images on the Acuson machine are conventional B-scan, but with the addition of specially modified green scale overlay. The green scale represents the standard

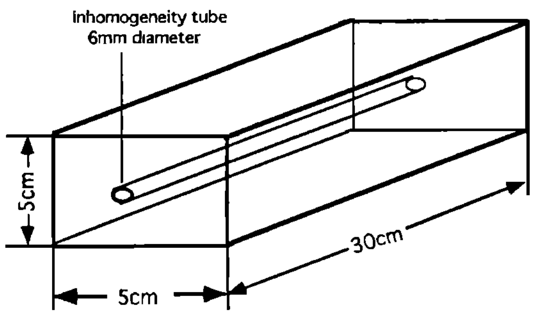

FIG. 5. Inhomogeneous phantom.

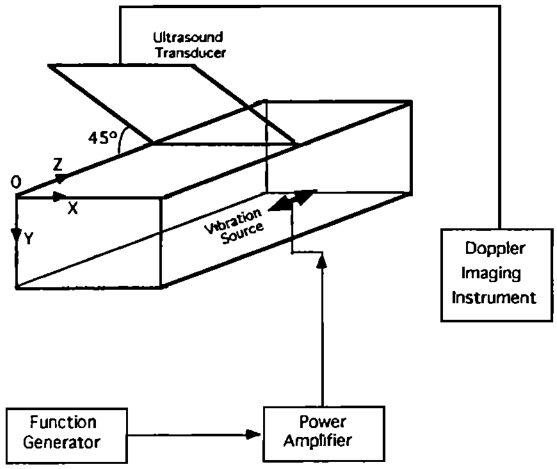

FIG. 6. Sketch of the experiment setup.

deviation of spread of Doppler spectrum, theoretically related to vibration amplitude (Huang, 1990). For any point on the image, if the green is on, it means that the vibration there is above threshold; if the green is off (normal speckle), it means that the vibration at that position is below threshold, which is approximately 0.02-mm displacement. Also, the brightness of the green scale is proportional to the amplitude of the vibration. For printing reproducibility, we converted the green images to black and white images for all the experiment results shown with normal B-scan speckle suppressed (lowered to dark gray values). Thus the brightness of the gray scale is proportional to the amplitude of the vibration. Some filtering with a small kernel has been applied to remove small artifacts due to noise. This gives a similar impression as watching a real-time image, where the noise tends to be averaged over sequential frames.

For the homogeneous phantom, the results of three different vibration frequencies, 59, 83, and 191 Hz, are given in Fig. 7. Clearly the 59-Hz excitation produces a 1:1 mode modal pattern; the 83-Hz excitation produces a 2:1 mode modal pattern; the 191-Hz vibration results in finer mode modal pattern.

For the inhomogeneous phantom, we show the images of two different vibration frequencies: 37 and 201 Hz (see Fig. 8). Notice the black middle upper part is just where the inhomogeneity was located, and that region shows a visible deficit of vibration.

B. Computer simulations

To check the validity of our theory, computer simulations were compared with the experiment results. The vibration plunger for the experiment was cone shaped; however, in computer simulations the boundary condition for that boundary was approximated as a Gaussian source. We assume this Gaussian source falls essentially to zero at the ends. The other three boundaries are rigid. The idea is demonstrated in Fig. 1.

1. Homogeneous case

The theory of the case two, a homogeneous, lossy medium, was used to calculate the vibration patterns for the homogeneous case study.

As the dimensions of our homogeneous phantom were 5.1 cm$\times$4.5 cm$\times$30 cm (width$\times$height$\times$length), so $L_a=5.1$ cm and $L_b=4.5$ cm. The lossy factor Q_0 was empirically set to 6.0. The speed of sound was set to 2.8 m/s, similar to the measured values found by Huang (1990). As the diameter of the tip of the vibration source was about 0.5 cm, and the homogeneous phantom had a width of 4.5 cm, the Gaussian source half-width parameter α was set to 0.5/4.5=0.11 (see case four in Sec. I for the definition of α). The results of the simulation at three different source frequencies are shown in Fig. 9. These modal patterns demonstrate a reasonable correspondence to those from the experiment in Fig. 7 over the vibration frequency range of 59–191 Hz.

2. Inhomogeneous case

The theory of case four, an inhomogeneous, lossy medium, was used to calculate the vibration patterns for the inhomogeneous phantom study.

As the dimensions of our inhomogeneous phantom were 5.1 cm$\times$5.0 cm$\times$30 cm (width$\times$height$\times$length), so $L_a=5.1$ cm and $L_b=5.0$ cm. The diameter of the inhomogeneity tube was 0.6 cm, so the tumor area $L_a'L_b'$ [defined in Eqs. (38) and (39)] was 0.283 cm^2. The inhomogeneity location

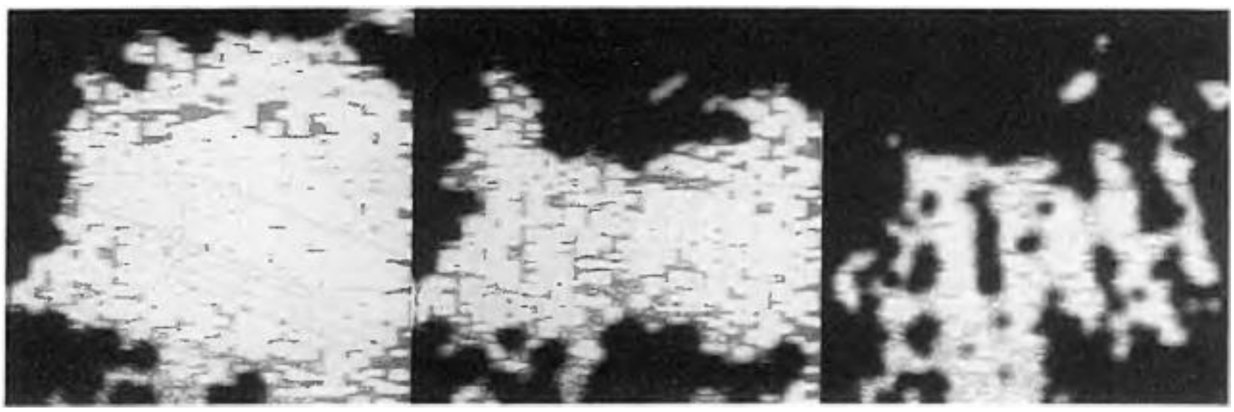

(a) (b) (c)

FIG. 7. Homogeneous phantom vibration pattern. The source vibration is located on the right-hand side of the images. Source vibration frequency is (a) 59, (b) 83, and (c) 191 Hz.

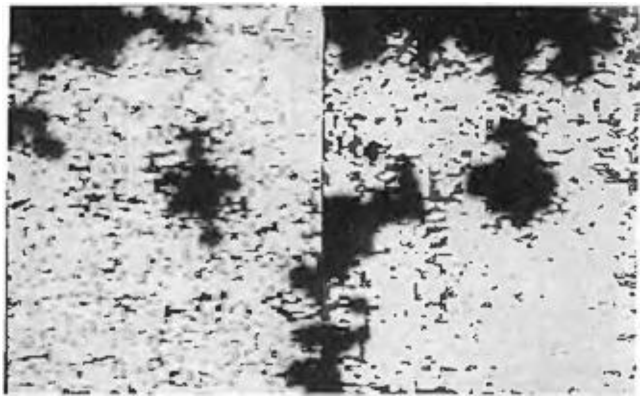

FIG. 8. Inhomogeneous phantom vibration pattern. The source vibration is located on the right-hand side of the images. The inhomogeneity is located on the middle upper part of the images, which shows little or no vibration (black area). Source vibration frequency is (a) 37 and (b) 201 Hz.

(x_0, y_0) was (3.0 cm, 2.3 cm). As the Young's modulus of the inhomogeneity was 4× that of the phantom, the γ in Eq. (13) was 3. The lossy factor Q_0 was empirically set to 3.0. The speed of sound was set to 2.8 m/s, and the Gaussian source width parameter α was set to 0.1. Equation (56) was used to generate the vibration amplitude. Notice that in Eq. (56) there are summations over p and q. These series were truncated at $p=q=30$. Looking at the expressions for A_{pq} and B_{pq} given by Eq. (39), the denominators are proportional to the fourth power of k_p and k_q, and the numerators are proportional to the square of k_p and k_q. When p and q are large enough so that k_p and $k_q \gg K$; also, k_p^2 and $k_q^2 \gg 1$, we could treat A_{pq} and B_{pq} as zero. In our case, K is always less than 660, while k_p and k_q are around 1800, when $p=q=30$; also k_p^2 and k_q^2 are greater than 10^6, so it is reasonable to approximate A_{pq} and B_{pq} as zero when p and q are above 30.

The theoretical results are shown in Fig. 10 for the same two frequencies as used in the Fig. 8 experiment. The inhomogeneity appears as a dark region, which indicates low vibration amplitude. The patterns are similar to those shown in the experiments.

C. Energy curve

In the phantom experiments, we varied the vibration frequency from 20 to 400 Hz, while keeping the amplitude of the vibration source constant. We noticed that the vibration response of the phantom was frequency dependent. At some frequencies, the phantom showed greater response to the applied vibration, producing an increase in the brightness and extent of the green scale overlay. In a homogeneous phantom the two strongest response peaks were observed at source frequencies of 37 and 56 Hz. Referring to the energy curve subsection of Sec. I, we calculated the theoretical energy response for the conditions of this experiment. Figure 11 shows the energy curve for the case where $L_a=5.1$ cm and $L_b=5.0$ cm; the lossy factor is $Q_0=3$, the speed of sound is 2.8 m/s, and the Gaussian source half-width parameter α is 0.1. We can see that the highest two peaks are predicted to be at 35 and 59 Hz, which closely matches the two peaks observed in the experiment.

D. Applications to *in vivo* imaging

To further examine the ability of our theory, we conducted a liver scan experiment on a volunteer from whom informed consent had been obtained. Low-frequency (about 20 Hz) vibration was applied to the right side of the midabdomen. The vibration was conducted into the liver. The vibration of the liver was sensed by a 3.5-MHz ultrasound transducer (V328) from Acuson (Mountain View, CA). The vibration image is shown in Fig. 12, where the sensitivity of the color imaging system was turned down so as to eliminate breathing and cardiac motion color.

The simulation model for the liver used the homogeneous model, case two in Sec. I, with a Gaussian source. L_b was taken to be 30 cm, and L_a was 10 cm. The lossy factor Q_0 was empirically set to 3.0. The speed of sound was set to 2.8 m/s. The Gaussian source half-width parameter α was set to 0.1. The simulation result is shown in Fig. 13. Although this model neglects the layered abdominal wall, the irregular liver shape, and ill-posed boundaries, comparing the results

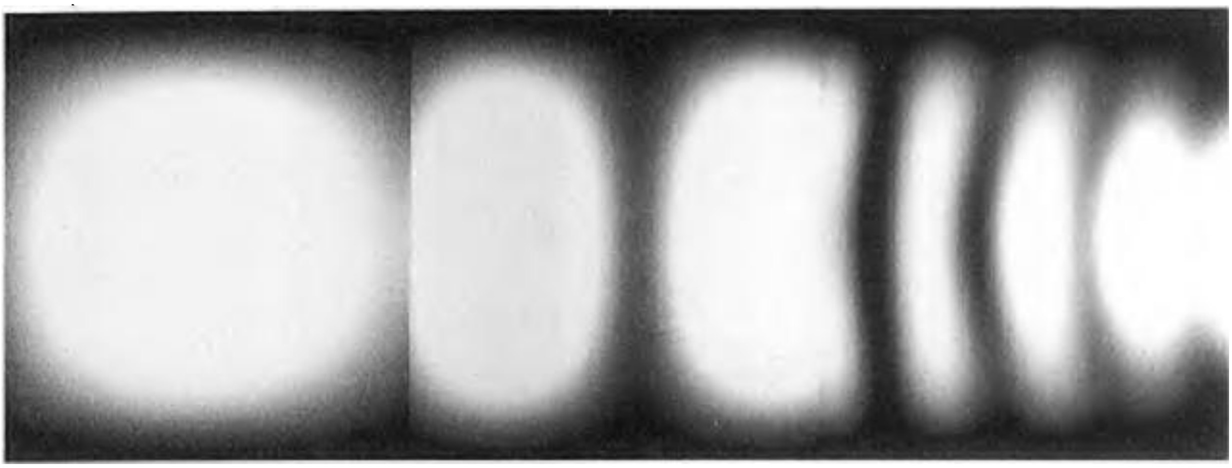

FIG. 9. Theoretical homogeneous vibration pattern. The source vibration is located on the right-hand side of the images. Source vibration frequency is (a) 59, (b) 83, and (c) 191 Hz.

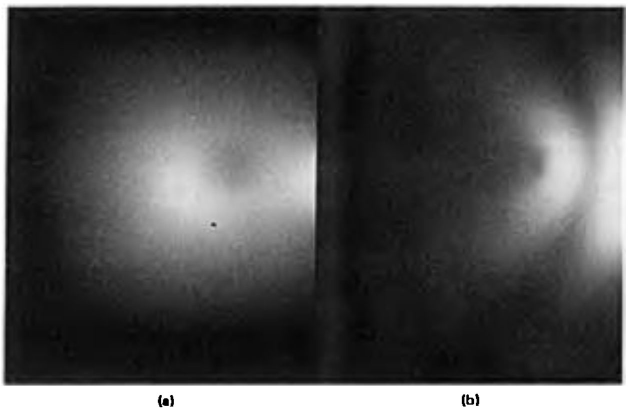

FIG. 10. Theoretical inhomogeneous vibration pattern. The source vibration is located on the right-hand side of the images. The inhomogeneity is located on the middle upper part of the images, which shows little or no vibration (black area). Source vibration frequency is (a) 37 and (b) 201 Hz.

with Fig. 12, the patterns are similar and display simple modal patterns that are indicative of vibration within a relatively homogeneous medium.

III. CONCLUSION

A basic model for sonoelasticity imaging is presented, using a "sonoelastic Born approximation" for shear waves in tissue with a small stiff tumor. Solutions are presented for two-dimensional cases with regular geometries. The results are encouraging for successful exploration and clinical application of sonoelasticity imaging. First, for the geometries and parameters given above, "tumors" with area as small as 0.005 of the surrounding tissue are detectable in ideal imaging circumstances assuming the tumor stiffness is at least a factor of 3 times greater than the surrounding "tissue." That is, the presence of the small tumor produces an approximate 20% drop in vibration amplitude. This is easily detectable in the "ideal" case where quantization noise from an 8-bit imaging system is the dominant noise. This assumption is well justified by previous studies such as Parker *et al.* (1990) and Huang (1990). This implies that, under ideal imaging conditions, a 3-mm stiff tumor can be visualized in a 5-cm organ such as the prostate. Second, the "energy curve" shows that low-order modes (which are easy to visualize and interpret) are easily produced by simple sources. Higher-order modes are more damped but have a very regular response over a range of frequencies. Both features may be useful in characterizing properties of the breast, liver and other organs using sonoelasticity imaging.

Sonoelasticity imaging was performed on phantoms and liver *in vivo*. Results were compared against theoretical predictions. The theory was found to satisfactorily predict the essential features of sonoelasticity imaging. These include

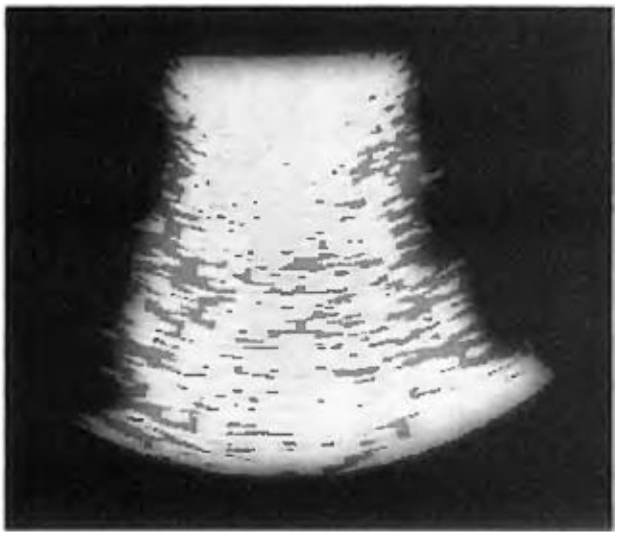

FIG. 12. Liver scan experiment. The orientation of the scan is such that the anterior abdominal muscles are located at the top of the image, the diaphragm at the bottom. Image shows only regions of vibration within the right lobe of a normal liver.

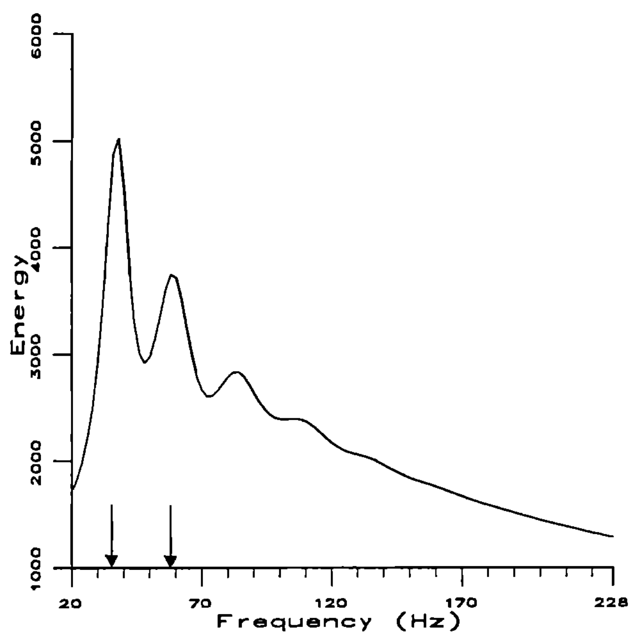

FIG. 11. Theoretical energy curve. The first two peaks (35 and 59 Hz, indicated by the arrows) were observed in experiment.

FIG. 13. Liver scan simulation using our theory for a homogeneous, bounded medium with a Gaussian vibration source.

the production of large well coupled modes at low vibration frequencies. Also, the disturbance produced by a discrete inhomogeneity is confirmed by theory and experiments. The whole liver has sufficiently homogeneous regions that can exhibit broad, low-frequency modal patterns. Both theory and phantom experiments might be useful in optimizing vibration and imaging systems such that small, discrete, hard tumors can be routinely identified in clinical applications of sonoelasticity imaging.

ACKNOWLEDGMENTS

The authors gained insight from discussions with Professor R. Waag, Dr. D. Rubens, and Dr. S. Huang. Loan of equipment from Acuson is gratefully acknowledged. The work was supported in part by the Department of Electrical Engineering, University of Rochester, and the NSF Center for Electronic Imaging Systems.

Adler, R., Rubin, J. M., Bland, P., and Carson, P. (1989). "Characterization of transmitted motion in fetal lung: Quantitative analysis," Med. Phys. 16, 333–337.

Adler, R. S., Barbosa, D. C., Cosgrove, D. O., Nassiri, D. K., Bamber, J. C., and Hill, C. R. (1990). "Quantitative tissue motion analysis of digitized *M*-mode images: Gestational differences of fetal lung," Ultrasound Med. Biol. 16, 561–569.

Axel, L., and Dougherty, L. (1989). "Heart wall motion: Improved method of spatial modulation of magnetization for MR imaging," Radiology 172, 349–350.

Birnholz, J. C., and Farrell, E. E. (1985). "Fetal lung development: Compressibility as a measure of maturity," Radiology 157, 495–498.

Céspedes, I., Ophir, J., Ponnekanti, H., and Maklad, N. (1993). "Elastography: Elasticity imaging using ultrasound with application to muscle and breast *in vivo*," Ultrason. Imaging 15, 73–88.

Cox, M., and Rogers, P. H. (1987). "Automated noninvasivemotion measurement of auditory organs in fish using ultrasound," J. Vib. 109, 55–59.

Dickinson, R. J., and Hill, C. R. (1982). "Measurement of soft tissue motion using correlation between *A*-scans," Ultrasound Med. Biol. 8, 263–271.

Eisensher, A., Schweg-Toffler, E., Pelletier, G., and Jacquemard, G. (1983). "La palpation échographique rythmée-echosismographie," J. Radiol. 64, 255–261.

Fung, Y. C. (1981). *Biomechanics—Mechanical Properties of Living Tissues* (Springer-Verlag, New York).

Gao, L., Alam, S. K., and Parker, K. J. (1993). "A new vibration theory for sonoelasticity imaging," *Proceedings of the 1993 IEEE Ultrasonics Symposium* 2 (IEEE, New York), pp. 879–882.

Gradshteyn, I. S., and Ryzhik, I. M. (1965). *Table of Integrals Series and Products*, translated from the Russian by Scripta Technica, Inc. (Academic, New York).

Holen, J., Waag, R. C., and Gramiak, R. (1985). "Representation of rapidly oscillating structures on the Doppler display," Ultrasound Med. Biol. 11, 267–272.

Huang, S. R. (1990). "Principles of sonoelasticity imaging and its applications in hard tumor detection," Ph.D. thesis, University of Rochester, Rochester, New York.

Javier, C. B., and Pedersen, C. P. (1994). "Ultrasonic measurement of forced diameter variations in an elastic tube," Ultrason. Imaging 16, 124–142.

Kinsler, L. E., Frey, A. R., Coppens, A. B., and Sanders, J. V. (1982). *Fundamentals of Acoustics* (Wiley, New York), pp. 90–91.

Krouskop, T. A., Dougherty, D. R., and Levinson, S. F. (1987). "A pulsed Doppler ultrasonic system for making noninvasive measurements of the mechanical properties of soft tissues," J. Rehabil. Res. Biol. 14, 1–8.

Landau, L. D., and Lifshitz, E. M. (1970). *Theory of Elasticity*, translated from the Russian by J. B. Sykes and W. H. Feid (Pergamon, New York), pp. 17–20.

Lee, F., Bronson, J. P., Lerner, R. M., Parker, K. J., Huang, S. R., and Roach, D. J. (1991). "Sonoelasticity imaging: Results *in vivo* tissue specimens," Radiology 181, 237–239.

Lerner, R. M., and Parker, K. J. (1987a). "Sonoelasticity imaging for cancer detection," in 12th International Symposium on Ultrasonic Imaging and Tissue Characterization, Alexandria, VA (unpublished).

Lerner, R. M., and Parker, K. J. (1987b). "Sonoelasticity images, ultrasonic tissue characterization and echo graphic imaging," in Proceedings of the 7th European Communities Workshop, Nijmegen, The Netherlands (unpublished).

Lerner, R. M., Parker, K. J., Holen, J., Gramiak, R., and Waag, R. C. (1988). "Sonoelasticity: Medical elasticity images derived from ultrasound signals in mechanically vibrated targets," Acoust. Imaging 16, 1988.

Lerner, R. M., Huang, S. R., and Parker, K. J. (1990). "Sonoelasticity images derived from ultrasound signals in mechanically vibrated tissues," Ultrasound Med. Biol. 16, 231–239.

Levinson, S. F. (1987). "Ultrasound propagation in anisotropic soft tissues: The application of linear elastic theory," J. Biomech. 20, 251–260.

Meunier, J., Bertrand, M., and Faouzi, K. (1989). "A model of speckle motion artifacts occurring under tissue linear transformation," Ultrason. Imaging 11, 133.

Morse, P. M., and Ingard, K. U. (1968). *Theoretical Acoustics* (McGraw-Hill, New York), p. 413.

O'Donnell, M., Emelianov, S. Y., Skovoroda, A. R., Lubinski, M. A., Weitzel, W. F., and Wiggins, R. C. (1993). "Quantitative elasticity imaging," *Proceedings of the 1993 IEEE Ultrasonics Symposium* 2 (IEEE, New York), pp. 893–903.

O'Donnell, M., Skovoroda, A. R., Shapo, B. M., and Emelianov, S. Y. (1994). "Internal displacement and strain imaging using ultrasonic speckle tracking," IEEE Trans. Ultrason. Ferroelectr. Frequency Control 41, 314–325.

Oestreicher, H. L. (1951). "Field and impedance of an oscillating sphere in a viscoelastic medium with an application to biophysics," J. Acoust. Soc. Am. 23, 707–714.

Ophir J, Céspedes, I., Ponnekanti, H., Yazdi, Y., and Li, X. (1991). "Elastography: A quantitative method for imaging the elasticity of biological tissues," Ultrason. Imaging 13, 111–134.

Parker, K. J., Huang, S. R., and Musulin, R. A. (1990). "Tissue response to mechanical vibrations for sonoelasticity imaging," Ultrasound Med. Biol. 16, 241–246.

Parker, K. J., and Lerner, R. M. (1992). "Sonoelasticity of organs: Shear waves ring a Bell," J. Ultrasound Med. 11, 387–392.

Parker, K. J., Huang, S. R., Lerner, R. M., Lee, F., Jr., Rubens, D., and Roach, D. (1993). "Elastic and ultrasonic properties of the prostate," *Proceedings of the 1993 IEEE Ultrasonics Symposium 2* (IEEE, New York), pp. 1035–1037.

Ponnekanti, H., Ophir, J., and Céspedes, I. (1992). "Axial stress distributions between coaxial compressors in elastography: An analytical model," Ultrasound Med. Biol. 18, 667–673.

Ryan, L K., Lockwood, G. R., Starkoski, B. G., Holdsworth, D. W., Rickey, D. W., Drangova, M., Fenster, A., and Foster, F. S. (1992). "A high frequency intravascular imaging system for investigation of vessel wall properties," *Proceedings of the 1992 IEEE Ultrasonics Symposium* 2 (IEEE, New York), pp. 1101–1105.

Ryan, L. K., Lockwood, G. R., Bloomfield, T. S., and Foster, F. S. (1993). "Speckle tracking in high frequency ultrasound images with application to intravascular imaging," *Proceedings of the 1993 IEEE Ultrasonics Symposium* 2 (IEEE, New York), pp. 889–892.

Skovoroda, A. R., Emelianov, S. Y., Lubinski, M. A., Sarvazyan, A. P., and O'Donnell, M. (1994). "Theoretical analysis and verification of ultrasound displacement and strain imaging," IEEE Trans. Ultrason. Ferroelectr. Frequency Control 41, 302–313.

Taylor, K. J. (1976). "Absolute measurement of acoustic particle velocity," J. Acoust. Soc. Am. 59, 691–694.

Taylor, K. J. (1981). "Absolute calibration of microphones by a laser-Doppler technique," J. Acoust. Soc. Am. 70, 939–945.

Trsitam, M., Barbosa, D. C., Cosgrove, D. O., Nassiri, D. K., Bamber, J. C., and Hill, C. R. (1986). "Ultrasonic study of *in vivo* kinetic characteristics of human tissues," Ultrasound Med. Biol. 12, 927–937.

Tristam, M., Barbosa, D. C., Cosgrove, D. O., Nassiri, D. K., Bamber, J. C., and Hill, C. R. (1988). "Application of Fourier analysis to clinical study of patterns of tissue movement," Ultrasound Med. Biol. 14, 695–707.

Von Gierke, H. E., Oestreicher, H. L., Franke, E. K., Parrack, H. O., and Von

Wittern, W. W. (1952). "Physics of vibrations in living tissues," J. Appl. Physiol. 4, 886–900.
Wilson, L. S., and Robinson, D. E. (1982). "Ultrasonic measurement of small displacements and deformations of tissue," Ultrason. Imaging 4, 71–82.
Yamakoshi, Y., Sato, J., and Sato, T. (1990). "Ultrasonic imaging of internal vibration of soft tissue under forced vibration," IEEE Trans. Ultrason. Ferroelectr. Frequency Control 37, 45–53.
Yemelyanov, S. Y., Skovoroda, A. R., Lubinski, M. A., Shapo, B. M., and O'Donnell, M. (1992). "Ultrasound elasticity imaging using Fourier based speckle tracking algorithm," *Proceedings of the 1992 IEEE Ultrasonics Symposium 2* (IEEE, New York), pp. 1065–1068.